

Relativistic and Electromagnetic Molecular Dynamics Simulations for a Carbon–Gold Nanotube Accelerator

Motohiko Tanaka, and Masakatsu Murakami¹

Graduate School of Engineering, Chubu University, Kasugai 487-8501, Japan

¹*Institute of Laser Engineering, Osaka University, Suita 565-0871, Japan*

December 14, 2024

Abstract

Relativistic molecular dynamics are described in ultra-high temperature and MeV energy behaviors. In strongly-coupled systems, Coulomb electrostatic potential is collected in the infinite space, and the electromagnetic fields are added in the coordinate space. Separation of the electrostatic and electromagnetic electric fields is a good approximation for short time periods. Computer parallelization for electromagnetic fields is applied. For a numerical application, a nanotube accelerator under an $E \times B$ pulse is investigated. Positive ions are accelerated in the parallel direction, whereas the electrons proceed in the perpendicular direction. Rapid expansion to infinite space and short-range electromagnetic radiation cooperate for large intensities. At $10^{22}\text{W}/\text{cm}^2$, pulsation oscillations for gold and carbon ions flare up, and electrons acquire the relativistic velocities. The energy of multiple gold ions reaches about 30 MeV, and the energy efficiency is 1%. They are observed in relativistic molecular dynamics simulation.

molecular dynamics simulation, Coulomb potential, separation of longitudinal and transverse parts, parallel computing, laser beam plasma production

1 Introduction

Ion accelerations driven by ultraintense and ultrashort laser pulses have been studied over the past two decades. Positive ion beams have wide applications such as tomography, cancer therapy [1], compact neutron sources [2], and ion-driven fast ignition for medicine [3]. To practically use accelerated ions, it is crucial to produce high-quality beams, which are monoenergetic and

collimated [4, 5, 6]. Laser-driven ion acceleration has been reviewed in the literature [7].

A temperature of 10^{10} K and a pulse duration of 10 fs are proposed for MeV-range accelerator physics. A molecular dynamics simulation suggested that a nanometer-sized nanotube can generate a quasi-monochromatic and directional beam of protons and carbon ions in the MeV energy range [8]. Additionally, a gold coating can be chemically adsorbed to the monolayer of carbon atoms, which comprise the carbon nanotube [9]. Low-Z materials such as hydrogen and carbon are fully ionized, while materials such as gold have mid-range ionization states $Z \leq 25$ at laser intensities of $\leq 10^{18}$ W/cm² [10]. Increasing the irradiated laser intensity by several orders of magnitude will be an interesting challenge as both the energy and energy efficiency must be increased above 10^{18} W/cm².

On the numerical simulations, the carbon nanotube accelerator should utilize molecular dynamics as inter-particle interactions are strong, like in polymer physics rather than in plasmas. The strongly-coupled system is defined by $\Gamma = e^2/\epsilon a k_B T > 1$ [11, 12], where e is a charge, ϵ is a dielectric constant, a is an inter-particle spacing, and $k_B T$ is thermal energy. The simulation in such systems is calculated with electrostatic forces, where the periodic Coulomb potential is by the use of the Ewald method for a large system at high accuracy [13]. The forces are $\exp(-(\gamma r)^2)/r$ in the short range, while the charge density with aliasing sums is convolved by a Fourier transform for the long range, with γ an inverse length parameter. The microwave heating of water shows that the ice state is crystallized and not melted below 273 K [14]. The other polymer fields are involved in the charge inversion and electrophoresis phenomena [15, 16, 17], DNA translocation in the nanopore [18], and macromolecules of polyampholyte [19].

In plasma physics, the electromagnetic simulations are treated in coordinate space on top of the finite-element method [20, 21]. The electromagnetic fields are calculated for high-beta plasmas, but the electrostatic field must be solved in coordinate space to avoid aliasing errors [22, 23]. They are applied to space physics [24, 25]. The codes are recently developed in robust moving mesh methods of time-dependent partial differential equations [26, 27]. Computation in Livermore National Laboratory is centered in many areas which are inertial confinement of laser fusion and computational mathematics on partial differential equations [28]. For the present carbon nanotube accelerator, however, the Γ parameter is highly variable at $\Gamma > 1$ for the initial phase and $\Gamma \ll 1$ for the expanded plasma in an unbound space. All particles in the infinite volume must be calculated by Coulomb potential field which was once done [29].

In the aforementioned study, a carbon nanotube was used in the relativistic molecular dynamics simulation. The simulation was used in the electrostatic approximation at that time. Fortunately, molecular dynamics simulations of today's technology can utilize real mass and charge particles with electromagnetic effects. The scalings of these ions and electrons can be addressed without additional adjustments.

The rest of this paper is organized as follows. In Sec.2, the methodology of molecular dynamics for relativistic and electromagnetic field simulations is described. A concise procedure, which separates the Coulomb potential and transverse electric fields, is a good approximation of small-scale phenomena. The Courant condition for electromagnetic fields is discussed in Sec.2.2. Parallel computing technique for molecular dynamics simulation will be discussed in Sec.2.3. Section 3 describes the numerical application of the molecular dynamics code. Protons, carbons, golds, and electrons are used at their real mass ratios, where the applied $E \times B$ Gaussian pulse in the time and space is given as $(\omega t - k_y y)$. The carbon nanotube is accelerated in the parallel and perpendicular directions for ions and electrons, respectively, and the energy efficiency is about 1% at 10^{22}W/cm^2 . Finally Sec.4 summarizes the paper.

2 Methodology of Relativistic Molecular Dynamics Simulations

2.1 Motion and Maxwell Field Equations

Solving the Newton equation of motion for position $\vec{r}(t)$ and velocity $\vec{v}(t)$ can realize time development in a system. Since particle positions of N particles are located in infinite space, the charged particles interactions must be highly accurate. It is contrary to using only the numerical grids in the coordinate space. The Coulomb potential is adopted in the equation of motion, which is written as,

$$\Phi_{Coul}(\vec{r}_i) = \sum_{j=1}^N q_i q_j / r_{ij}. \quad (1)$$

Here, q_i is the i^{th} particle charge, r_i is the position in the parallel (z) and lateral directions (x and y). The vector $r_{ij} = r_i - r_j$ is the displacement between the i^{th} and j^{th} particles. The sum of all possible combinations of particles must be specified. (Refer to Appendix A for the international system of units.)

In nanometer crystals in general, particles have strong short-range interactions. These interactions can be represented by the Lennard-Jones potential, which is expressed as,

$$\Phi(r_i, r_j) = \epsilon_{ij}[(\sigma_{ij}/r_{ij})^{12} - 2(\sigma_{ij}/r_{ij})^6]. \quad (2)$$

The short-range potential is repulsive if the distance between the two particles is small, but is attractive if the particle distance is larger than the equilibrium distance. The potential for carbon pairs has an equilibrium at $\sigma_{CC} = 1.421\text{\AA}$ and $\epsilon_{CC} = 4\text{eV}$ ($1\text{eV} = 1.602 \times 10^{-12}\text{erg}$). Hence, a solid six-membered network of nanotubes is created. The other ions are weakly dependent, and their potentials are assumed to be null, $\epsilon_{AuAu} = 0$. Actually, the depth of the carbon potential is about $T \approx 4 \times 10^4\text{K}$. Consequently, the short-range potential works to initially form a nanotube crystal. Within the $10\text{-}\text{\AA}$ pairs, the Coulomb and Lennard-Jones interactions are calculated at a small time step Δt , while the interactions beyond that range are kept at $5\Delta t$.

The electromagnetic interactions are calculated by a set of Maxwell equations in rectangular coordinates. Usually, the retarded potential is used for the special relativity [30, 31]. Although this potential is difficult to solve for a system with a large number of particles, such as $N > 10^5$ particles, the large Coulomb potential field and the transverse electric field are separated. This separation is possible since the physical process is contained in small scale of 100 nm of the accelerated nanotube, in which the light travels one-tenth of the period (about 0.3 fs) for an 800-nm sapphire laser.

Finite coordinate grids for electromagnetic fields are used to define the transverse electric field $\vec{E}_T(\vec{r}, t)$ and the magnetic field $\vec{B}(\vec{r}, t)$. The transverse electric field \vec{E}_T is prescribed in that the transverse \vec{j}_T and longitudinal \vec{j}_L parts are separated. The longitudinal electric field \vec{E}_L is first solved in the coordinate space by

$$\nabla \cdot \vec{E}_L(\vec{r}) = 4\pi \sum_{i=1}^N q_i S(\vec{r} - \vec{r}_i). \quad (3)$$

The summation is taken over particles and $S(\vec{r})$ is prorated to nearby grids (the shape function is $S(\vec{0}) = 1$ and $S(\vec{r}) \rightarrow 0$ when $|\vec{r}| \gg \Delta x$). The real-even function *sine* of the fast Fourier transform [32] is used as $\vec{E}_L(\vec{r}) = -\nabla \Phi_L(\vec{r})$ and $\Phi_L(\vec{r}) \propto \sin(k_x x) \sin(k_y y) \sin(k_z z)$. The transverse part is separated from the longitudinal part, which is given by

$$\vec{j}_T = \vec{j} - (\vec{j} \cdot \vec{E}_L)/|\vec{E}_L|. \quad (4)$$

Here, the current density \vec{j} is summed over the charge and velocity of the particles as

$$\vec{j}(\vec{r}) = \sum_{i=1}^N q_i \vec{v}_i S(\vec{r} - \vec{r}_i). \quad (5)$$

The time step for the \vec{E}_T and \vec{E}_L fields is $t = t^{n+1/2}$, where t^α stands for the time level $t = t^\alpha$. After this separation, the Coulomb potential and electromagnetic fields are used in Eq.(10) below, instead of the longitudinal electric field for the resolution accuracy. The electromagnetic fields are solved in the coordinate, which are due to the available meshes from computer resources.

The electromagnetic fields are determined by the Maxwell equation. Round differential derivatives of space $\nabla \times$ and time $\partial/\partial t$ are the centered differential scheme, which is given by

$$(1/c)\partial\vec{B}/\partial t = -\nabla \times \vec{E}_T, \quad (6)$$

$$(1/c)\partial\vec{E}_T/\partial t = \nabla \times \vec{B} - (4\pi/c) \sum_{i=1}^N q_i \vec{v}_{T,i} S(\vec{r} - \vec{r}_i), \quad (7)$$

$$\nabla \cdot \vec{B} = 0, \quad (8)$$

with $\vec{B} = \vec{H}$ in the CGS system of plasmas. The time advance is $t^{n-1/2} \rightarrow t^{n+1/2}$ for the magnetic field \vec{B} . The separation of the \vec{j}_T component from the current \vec{j} is done at $t^{n+1/2}$, and the transverse electric field \vec{E}_T is advanced by $t^n \rightarrow t^{n+1}$. The space operator of three dimensions, for example the electric field, is given by

$$\begin{aligned} \nabla \times \vec{E} = & (\partial E_y / \partial z - \partial E_z / \partial y, \partial E_z / \partial x - \partial E_x / \partial z, \\ & \partial E_x / \partial y - \partial E_y / \partial x). \end{aligned} \quad (9)$$

The relativistic equation of motion to define momentum \vec{p}_i , position \vec{r}_i , and velocity \vec{v}_i , is written by the centered ordinary differential scheme as,

$$\begin{aligned} d\vec{p}_i/dt = & -\nabla \sum_{j=1}^N [q_i q_j / r_{ij} + \Phi(r_i, r_j)] \\ & + q_i [\vec{E}_T(\vec{r}_i, t) + (1/c) \vec{v}_i \times \vec{B}(\vec{r}_i, t)], \end{aligned} \quad (10)$$

$$d\vec{r}_i/dt = \vec{v}_i, \quad \vec{p}_i = m_i \vec{v}_i / \sqrt{1 - (\vec{v}_i/c)^2}. \quad (11)$$

The electrostatic terms in the first bracket, namely Eq.(1) and Eq.(2), and the electromagnetic terms in the second bracket, Eq.(10), are used here.

Here, m_i is the mass of the i^{th} particle, c is the speed of light, the symbol d/dt is the full time derivative, and ∇ is an operator $(\partial/\partial x, \partial/\partial y, \partial/\partial z)$. The time advance for the momentum \vec{p} is made at $t^n \rightarrow t^{n+1}$, and that for the position \vec{r} is by a half-time staggered at $t^{n+1/2} \rightarrow t^{n+3/2}$.

The coordinate space has the meshes centered at the origin. The grids of 5 Å have spacing $(500)^2 \times 1000$ Å³ in $\vec{E}_T(\vec{r}_i)$ and $\vec{B}(\vec{r}_i)$ in the x, y and z directions for $< 10^{21}$ W/cm², but must have $(500)^2 \times 1500$ Å³ for large intensity 10^{22} W/cm². In the external regime, other components are null except for $(-\nabla\Phi)$ in Eq.(1) and the drift terms $(E_{z,0}, B_{x,0})(\vec{r}, t)$. The Gaussian pulse with an 800-nm wavelength (2.67×10^{-15} s) is induced from the negative y direction toward the origin at the speed of light. It decays in $\Delta Y = 2.8\mu\text{m}$ in the y direction, namely $3.5 \times 800\text{nm}$, and $\Delta X = 0.1\mu\text{m}$ in the x, y directions,

$$\begin{aligned} E_{z,0}(\vec{r}, t) &= E_0 \sin(\omega t - k_y y) * f_n, \\ B_{x,0}(\vec{r}, t) &= B_0 \cos(\omega t - k_y y) * f_n, \end{aligned} \quad (12)$$

and the slope f_n is

$$f_n = \exp[-((y - p_{xyz})^2/\Delta Y^2 + (x^2 + z^2)/\Delta X^2)]. \quad (13)$$

Here, the oscillation frequency is $\omega = ck_y$, and $E_0 = B_0$. The slopes are $p_{xyz} = (-3 + t/2.67 \times 10^{-15}) \times 800\text{nm}$, $\Delta Y = 2.8\mu\text{m}$ (3.5 wave periods) and $\Delta X = 0.1\mu\text{m}$. The time step is $\Delta t = 5 \times 10^{-19}$ s. The laser intensity 5×10^{17} W/cm² corresponds to the electric field 1.46×10^{12} V/m in the MKSA unit, which is 4.58×10^7 statV/cm in the CGS unit. (Refer to Appendix A for the international system of units.)

One points out that the electrostatic field must be solved with the electromagnetic fields because aliasing errors of latter grids can be finite [22]. Multiple nanotubes in Runs B1 and B2 are optimized simulations to be shown at the end of Sec.3.2. The electrostatic simulation for low intensities will be presented in Appendix B.

2.2 Ionization state and Courant condition

The values studied in this simulation range between 10^{16} to 10^{22} W/cm². The carbon nanotube on the surface of the two-dimensional cylinder surface is about 15 nm (radial, diameter) and 30 nm (height, diameter). The gold ions are set by 2-Å positions outside of the accompanying carbon pairs. Moreover, inside the inner cylinder, the bulk, which has a 12-nm diameter and 27-nm full length (height), is uniformly filled with protons and electrons.

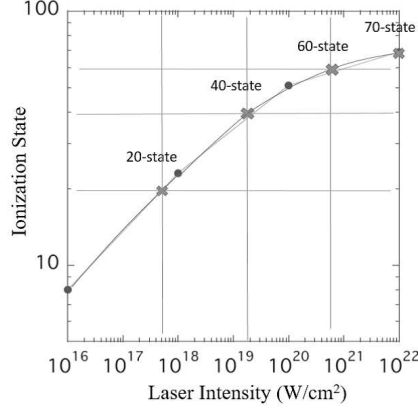


Figure 1: Laser intensity and ionization state of gold ions for $10^{16} - 10^{22} \text{W/cm}^2$.

The proton and carbon ions are fully ionized due to the high laser intensity. On the other hand, the gold ions are partially ionized, depending on the laser intensity [10], as depicted in Fig.1. Each run is assigned an ionization state, $Z_{is} = 20, 40, 60$, and 70 , which are designated as Run A1, A2, A3, and A4, respectively.

The plasma contains: (i) carbon ions with six ionization states and 55,000 particles, (ii) gold ions as described above with 55,000 particles, (iii) protons with a single ionization state and 10,000 particles, and (iv) electrons with a negative single ionization state. The charge neutrality condition determines the number of electrons. Particles (4.1×10^5) are assigned as protons, carbons, golds, or electrons. The initial temperature of the particles is equal to null. Run A1 to A3 are executed as long runs with $t = 41\text{-}60$ fs with $L_z = \pm 500 \text{\AA}$. Run A4 arises a rapid expansion which subsides and lasts $t \leq 25$ fs, and full electromagnetic fields require the space accuracy at $\Delta x = 2.5 \text{\AA}$ with $L_z = \pm 750 \text{\AA}$. The particles without protons are executed as the similar accuracy for Run B.

To minimize the number of electrons, the electrons are disguised such that electrons are lumped up as super-electrons with a super-charge and mass of $e_\alpha = -\alpha e$ and $m_\alpha = \alpha m_e$. One super electron with $e_\alpha = -6e$ is assigned to a carbon ion. For gold, one super electron with $e_\alpha = -5e$ is assigned to one-fourth of the gold ions for Run A1. In the same token, one super electron with $e_\alpha = -10e$ is assigned to one-fourth of the gold ions for Run A2, one electron $e_\alpha = -15e$ is assigned to one-fourth of the gold ions for Run A3, and one super electron with $e_\alpha = -70/4e$ is assigned to

one-fourth of the gold ions for Run A4. A positive ion, namely a proton, carbon, or gold, is used as the independent normal particle.

The Courant-Friedrichs-Lewy condition must be satisfied for the numerical code to be stable for electromagnetic waves [33]. The time step Δt and grid interval Δx must be greater than the speed of light,

$$\Delta x/c\Delta t > 1, \quad (14)$$

otherwise the simulation blows up immediately for the explicit code. The most demanding condition for Run A4 with 2.5 \AA should be

$$\Delta x/c\Delta t = 2.5 \times 10^{-8} \text{ cm}/c \times 5 \times 10^{-19} \text{ sec} = 1.67, \quad (15)$$

which satisfies the aforementioned condition.

2.3 Parallel computing in electromagnetic fields

The molecular dynamics simulation runs for the Coulomb potential and electromagnetic field calculations. The $N \times N$ particle summation of the Coulomb potential field is well parallelized which is as fast as 94% computation efficiency. On average, it is 3.68 s per time step for Run A4 of 100 ranks, 16 processors and 14 GB per processor using the OpenMP technique of Fujitsu FX100. The total elapsed time of 4.2×10^5 particles for Run A4 consumes 51 hours for the 5×10^4 time steps, that is equal to physical run of 2.5×10^{-14} s. The redundant computation for the electromagnetic fields ($200^2 \times 600$ meshes), the electromagnetic and electrostatic field separation by octa-threading, the particle advances, and small operations becomes 2.67 s out of the aforementioned average execution time.

The electromagnetic fields can be parallelized by the use of domain decomposition in the coordinate space, when a large number of processors are to be used. Different electromagnetic fields in each segments are allocated in local memory with a minimal overlap of nearby processors. One-dimensional (z) field arrays are handled with *mpi_isend/mpi_irecv* subroutines. Each processor calls the magnetic and transverse electric fields in Eq.(6) and Eq.(7), with additional slight smoothing of the fields. A redundant execution of the electromagnetic fields and the particle advances, which is 1.44 s per time step out of 2.67 s mentioned above for $\Delta x = 2.5 \text{ \AA}$, is reduced to 0.18 s for parallel 52 ranks per time step.

Thus, parallelization makes simulation with more resolution accuracy. For the resolution of $\Delta x = 1.67 \text{ \AA}$ and total of $(300)^2 \times 936$ meshes ($(500)^2 \times 1500 \text{ \AA}^3$), for example, the Courant condition is satisfied $\Delta x/c\Delta t = 1.11$.

Table 1: The kinetic energy of carbons, golds, protons and electrons (MeV, average) for the laser intensity in Runs A1 to A4 (W/cm^2). The energy efficiency of golds over electrons (%) is also listed.

Series	laser intensity	C	Au	Proton	electron	Efficiency
A1	5.0×10^{17}	0.32	0.59	0.085	0.036	69%
A2	1.7×10^{19}	0.76	6.0	0.21	0.53	25%
A3	6.0×10^{20}	0.82	13.9	0.25	6.1	3.1%
A4	1.0×10^{22}	3.0	21.9	0.50	38.0	0.76%

Table 2: The carbon, gold and electron energies (MeV, average), and energy efficiency of golds to electrons (%) for the number of gold layers within a nanotube. Quotation to Run A4 for the single cage (with protons) is shown as the first line.

Series	layers	C	Au	electron	Efficiency
A4	1	1.0	19.8	39.7	0.65%
B1	2	2.0	23.5	29.6	0.46%
B2	3	2.3	28.9	50.8	0.97%

The local memory is 10 GB per processor, and its timing is 3.58 s per time step for the 52 ranks with the Coulomb potential calculation of 1.42 s included. A redundant execution in the field separation, that is written in Eqs.(3)-(5), is also included as 1.76 s for the 52 ranks .

3 Carbon nanotube accelerator assisted by gold ions

3.1 Time developments of ions and electrons

Table 1 shows the results for Run A1 to A4, which have a laser intensity of 10^{16} – $10^{22} \text{W}/\text{cm}^2$. Each run is initiated with a Gaussian pulse at the leftward position $y = -3.5 \times 800 \text{ nm}$. A laser shot radiates the nanotube sideways from the lateral direction.

Figure 2 depicts the laser intensity of $5 \times 10^{17} \text{W}/\text{cm}^2$ for Run A1 with a time development of nanotube expansion of (a) 13 fs, (b) 20 fs, and (c) 45 fs for the yz plots, and (d) the reduced yx and yz plots with the electrons at 45 fs. Laser irradiation induces a sudden rapid expansion of all

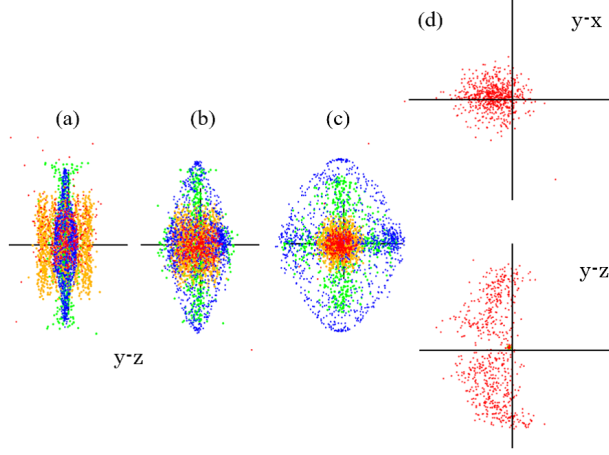


Figure 2: (Color) The time sequence of $5 \times 10^{17} \text{ W/cm}^2$ (Run A1) for enlarged yz plots at (a) 13fs, (b) 20fs, (c) 45fs, and (d) for the reduced yx and yz plots, mostly of electrons, in 45fs. Protons are shown in blue, carbons by green, golds by gold, and electrons in red. The scales are $3.3 \times 10^{-6} \text{ cm}$, $5.5 \times 10^{-6} \text{ cm}$, $1.6 \times 10^{-5} \text{ cm}$ in (a) to (c), respectively, and $9.4 \times 10^{-4} \text{ cm}$ in two vertical plots (d).

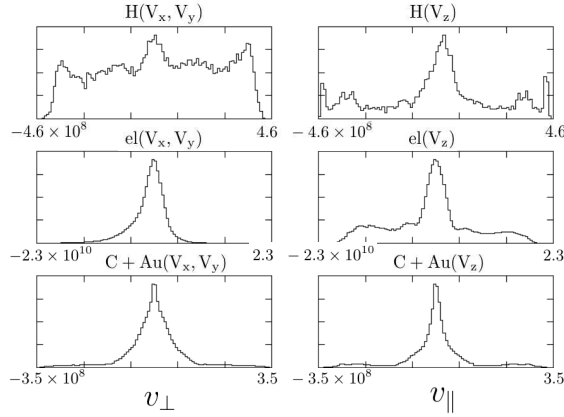


Figure 3: The velocity distribution functions of protons, electrons, and carbon plus gold ions for Run A1 (from the top to bottom panels), respectively. A time is 40fs for the perpendicular direction (V_x, V_y) (left), and the parallel direction V_z (right), with c the speed of light in cm/s. Scales are 4.6×10^8 , 2.3×10^{10} , and $3.5 \times 10^8 \text{ cm/s}$ from protons, electrons, and carbons plus golds, respectively, and ordinates in linear scales are arbitrary.

ions. The antecedent protons (blue) are accelerated in the parallel (z) and perpendicular directions of the nanotube cylinder, as seen in panels (a) - (c). The carbon (green) and gold ions (gold) are chasing protons like guard spears, and the acceleration of positive ions lasts for $t > 45$ fs. On the other hand, as the electron mass is quite light $m_e \ll m_i$ (red), the electrons move around 100 times more for a larger space than the positive ions. The electrons are spread wider than the ions, but they are limited to $10\mu\text{m}$ and have a double-humped yz profile with $y \leq 0$ in the panel (d).

Figure 3 depicts the velocity distribution functions for Run A1. There is a main central peak which extends with a tail formation for protons and electrons at $5 \times 10^{17}\text{W}/\text{cm}^2$. The protons have positive and negative tails in V_{\parallel} and V_{\perp} directions. These tails are somewhat higher in the V_{\perp} direction. Carbon and gold ions have only thin tails, whereas electrons have thick tails in the both V_{\parallel} directions.

The electron has a rest energy of 0.51 MeV [34], whose kinetic energy of the same amount may be declared in the entry of the relativistic regime. It is $1 \times 10^{19}\text{W}/\text{cm}^2$ for the carbon and gold accelerator, listed in Table 1. At $1.7 \times 10^{19}\text{W}/\text{cm}^2$ (Run A2), the order of energy is the first gold ions which follow carbons and electrons in the geometry space. The electrons develop a spiral shape outside the positive ions, and occupy both positive and negative z coordinates. It will be verified by distributions of the ions to the parallel direction in Fig.7.

At $6 \times 10^{20}\text{W}/\text{cm}^2$ (Run A3), a large spiral, which resembles a semi-arc shape, occupies the negative z direction. The gold ion peak increases to 11.6 MeV, and the electrons have a second energy position at 6.1 MeV; carbon ions fall down to the third energy position 0.68 MeV. Regardless of the order, the carbon ions are the most important component because the six-membered cage of the nanotube must be supported initially.

At $1 \times 10^{22}\text{W}/\text{cm}^2$, all the ions and electrons flare up in massive electromagnetic radiation in Fig.4 (Run A4). A new simulation with meshes of $|x| \leq 500\text{\AA}$ and $|z| \leq 1000\text{\AA}$ (5\AA intervals) covers the rectangular meshes of the electromagnetic interactions. Fast pulsation oscillations occur for the gold and carbon ions in the phase $t \cong 10$ fs. The maximum energy is 23.6 MeV at $t \cong 11$ fs, and the final energy is 19.8 MeV. The energy of the gold ions are moderated compared with the large fictitious electrostatic simulation of 40 MeV. The electrons are completely separated from all the ions, and proceed in the $E \times B$ drift toward the $y > 0$ direction. Their velocities are nearly 90% that of the speed of light. The energy of the electrons is 39.7 MeV.

The velocity distribution functions shows again the pulsation oscillations

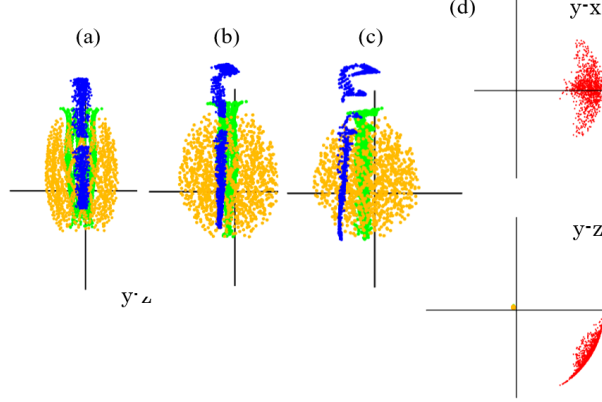


Figure 4: (Color) The time sequence of $1 \times 10^{22} \text{W/cm}^2$ (Run A4) for enlarged yz plots at (a) 5fs, (b) 11fs, (c) 25fs, and (d) for reduced yx and yz plots, mainly of electrons, at 25fs. Protons are shown in blue, carbons by green, golds by gold, and electrons in red. The scales are $5.8 \times 10^{-6} \text{cm}$, $1.2 \times 10^{-5} \text{cm}$ and $3.1 \times 10^{-5} \text{cm}$ in (a) to (c), respectively, and $7.4 \times 10^{-4} \text{cm}$ in two vertical plots (d).

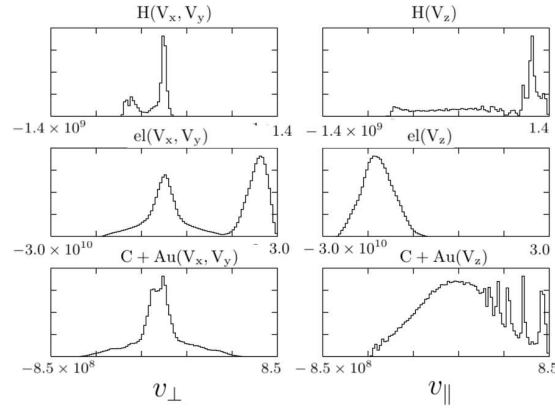


Figure 5: The velocity distribution functions of protons, electrons, and carbon plus gold ions for Run A4 (from the top to bottom panels), respectively. A time is 23fs for the perpendicular direction (V_x, V_y) (left), and the parallel direction V_z (right), with c the speed of light in cm/s. Scales are 1.4×10^9 , 3.0×10^{10} , and $8.5 \times 10^8 \text{cm/s}$ from protons, electrons, and carbons plus golds, respectively, and ordinates in linear scales are arbitrary.

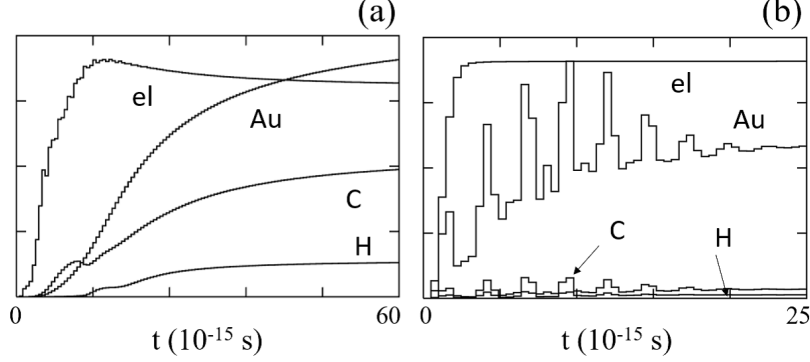


Figure 6: The time changes of kinetic energy of golds, carbons, protons, and electrons for (a) $5 \times 10^{17} \text{ W/cm}^2$, and (b) $1 \times 10^{22} \text{ W/cm}^2$. The maximum values are, (a) 0.59 MeV for ions (C,Au,H), and 0.33 MeV for electrons, (b) 34.1 MeV for golds, and 38.0 MeV for electrons, respectively. The final value of gold ions is 21.9 MeV for (b).

for the gold ions in Fig.5. The proton distribution function of V_{\parallel} is widely distributed from the maximum positive to the negative parts. Protons in the parallel direction have a velocity at $1.4 \times 10^9 \text{ cm/s}$ and are broadly distributed from the top and bottom portions, $(-1 \sim 1.4) \times 10^9 \text{ cm/s}$. The carbon and gold ions in V_{\parallel} have half the velocity of the protons. The population centered at $8 \times 10^8 \text{ cm/s}$ in the parallel direction is due to the carbon ions, while that centered at $3 \times 10^8 \text{ cm/s}$ is due to the gold ions. The electrons are relativistic where the V_y decentered plot shows $(-2 \sim -3) \times 10^{10} \text{ cm/s}$ in the middle of Fig.5 (superpositions of the central distribution in V_x and the decentered one in V_y are shown). The decentered electron distribution was also presented in the bottom yz plot of Fig.4(d).

3.2 Behavior of energy and efficiency

The momentum and energy of each particle reveal the acceleration behavior of plasmas. The momentum of the species with N_s particles is defined by $W_{kin,s} = \sum_{i=1}^{N_s} (\vec{p}_i^2 / 2m_i)$. The total momentum determines the course of the dynamical system. The separate behavior of the ions or electrons is highlighted, which is divided by N_s as $w_{kin,s} = \sum_{i=1}^{N_s} (\vec{p}_i^2 / 2m_i) / N_s$.

The energies of the golds, carbons, and protons increase monotonically in Run A1 of Fig.6(a). The gold ions grow twice as fast as the carbon ions at 45 fs, and the electric interactions with these heavy ions are important.

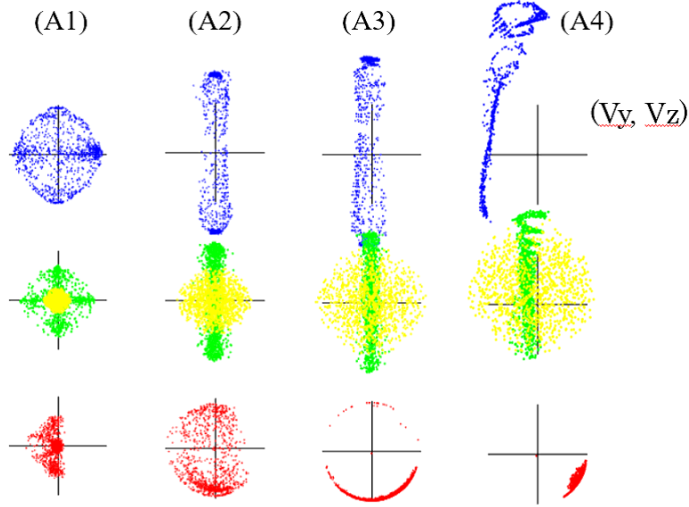


Figure 7: (Color) The 2D velocity plots of (i) protons, (ii) carbons and golds, and (iii) electrons, from the top to bottom panels, respectively. The times for Run A1 to A4 are, (a) 45fs, (b) 35fs, (c) 35fs, and (d) 25fs. The plot scales are, 100 times in the top row (for protons, blue), 50 times in the middle row (for carbon, green, and gold, gold), and 1.5 times for the bottom row (for electrons, red).

However, the growth of the protons is one order of magnitude smaller than that of heavy ions. The electrons become saturated around $t=12$ fs, but their growth is still half of that for the gold ions for Run A1. The energies on the average are 0.55 MeV for golds, 0.30 MeV for carbons, 0.082 MeV for protons, and 0.33 MeV for electrons.

Figure 6(b) shows the time change of the energy for Run A4, where a fine mesh $\Delta x = 2.5\text{\AA}$ is executed by $|x| \leq 250\text{\AA}$ and $|z| \leq 750\text{\AA}$. There occurs enormous growth of electromagnetic radiation at short ranges, and observed maxima are 34.1 MeV for golds and 3.0 MeV for carbons at $t \cong 10$ fs. The energy of the electrons is 99% of the total energy as early as 2 fs, and its energy becomes 38.0 MeV for the entire time of $t > 4$ fs. A deceleration of positive golds and carbons is then followed in a later stage, and the gold ions converge to 21.9 MeV at $t = 25$ fs. The proton energy is fairly small because its mass is about 200^{-1} that of the gold ions. On the other hand, the $\Delta x = 2.5\text{\AA}$ spacing for Run A3 is almost the same consequences in the entire regime with the $\Delta x = 5.0\text{\AA}$ run.

Figure 7 compares the velocity distributions in the (V_y, V_z) space for

Runs A1 - A4. For Run A1, the protons, carbons, and golds are symmetric in (V_y, V_z) of the first two rows of panel (a). The electrons in the third row occupy mainly the leftward hemisphere V_y , and both the top and bottom parts resemble a butterfly pattern in the V_z direction. Run A2 in panel (b) is symmetric for the positive ions and the distributions are straight up toward the parallel direction. The electrons form a large arc in the entire $V_y - V_z$ space. The energy of $10^{19}\text{W}/\text{cm}^2$ is the beginning of the relativistic regime, as panel (b) of Fig.7. For Run A3 in (c), the electrons form an antisymmetric arc, which appears quite large mostly in the negative regime, $V_z < 0$. Finally, for Run A4 in (d), the pipe shape for the protons is totally antisymmetric, and the electrons exhibit a very large island in the fourth quadrant with $V_y > 0$ and $V_z < 0$.

The momentum elucidates the energy efficiency. The momenta of Run A1 are 17.2%, 31.9%, 0.86%, and 50.1% for carbons, golds, protons, and electrons, respectively. All ions and electrons are almost the same amount divided, and the ratio of golds to electrons is $(\text{Au}/\text{electron}) = 64\%$. As the laser intensity increases from Run A2 to Run A3, the energy efficiency of the ions drops exponentially. The energy efficiency of the golds to electrons for Run A3 becomes 3.1%. At the large intensity Run A4, the ratios are $3.4 \times 10^{-4}\%$, 0.65%, $2.4 \times 10^{-5}\%$ and 99.4% for carbons, golds, protons, and electrons, respectively. The ratio of golds to electrons is $(\text{Au}/\text{electron}) = 0.65\%$.

The trend for the kinetic energy over the intensity $> 10^{20}\text{W}/\text{cm}^2$ shows that the gold ions are approaching parabolic sub-relativistic in Table 1. It is compared to a linear relativistic regime for the electrons.

Good optimizations are executed at $1 \times 10^{22}\text{W}/\text{cm}^2$ in Table 2. The $E \times B$ drift speed remains the same as before. The cylindrical nanotube of the single cage in Run A is built up for a double or triple cages in Run B. The rapid fast oscillations of gold ions are subsidized by $t < 20$ fs, and the energy at the final time is about 70% of the maximum value at 10 fs. The final value for the double-stacked cylindrical cage is 23.5 MeV (Run B1, on the average), while that of the triple-stacked cylindrical cage is 28.9 MeV (Run B2). The calculated energy efficiencies for the double and triple-stacked cages are $(\text{Au}/\text{electron}) = 0.46\%$ and 0.97%, respectively.

4 Summary

Relativistic and electromagnetic molecular dynamics was described for ultra-high temperature and a few tens of MeV behaviors. Highly accurate interactions were executed to real charge and mass of particles. The Coulomb

potential was collected in the infinite space, and the electromagnetic fields were calculated in the coordinate space. The transverse part of current from the longitudinal one was separated as a good approximation, because the physical process was contained in 100 nm of the accelerated nanotube; the light travels over one-tenth of the period of an 800-nm (2.7fs per period) sapphire laser.

As the relativistic molecular dynamics simulation, the nanotube accelerator was performed using the Coulomb potential and electromagnetic fields with 100 ranks \times 16 processors. With the $E \times B$ pulse of 800 nm, the positive ions were accelerated in homogeneous directions in the $5 \times 10^{17} \text{W/cm}^2$ range. Exceeding the 10^{18}W/cm^2 range, the relativistic regime appeared clearly and the ions were straight in the parallel direction, whereas electrons were asymmetric and proceeded in the oblique direction. At the large intensity 10^{22}W/cm^2 , the massive electromagnetic radiation for short ranges and the rapid expansion to the infinite space were present in the simulation. The gold and carbon ions were flared up at pulsation oscillations, and electrons acquired 99% of the speed of light. The energy of multiple gold ions reached about 34 MeV, and the energy efficiency was 1%.

The summary is that the numerical simulation method was presented for ultra-high temperature and a few tens of MeV behaviors. The simulation code was utilized in Coulomb potential and electromagnetic fields, which was examined for resolution accuracy. It was the cooperation of Coulomb potential and electromagnetic radiation of plasmas in the relativistic molecular dynamics simulation.

Acknowledgments

One of the authors (M.T.) would like to thank Professor A. Iiyoshi, Professor M. Sato and Professor Y. Zempo for kindness, and physics and computational discussions. The present simulations were performed using Fujitsu FX100 Supercomputer at the National Institute for Fusion Science, Japan.

Appendix A: Motion and Maxwell Field Equations by the International System of Units

The equation of motion for plasmas is written in the international system of units as,

$$d\vec{p}_i/dt = -\nabla \sum_{j=1}^N [q_i q_j / 4\pi\epsilon_0 r_{ij} + \Phi(r_i, r_j)] + q_i [\vec{E}_T(\vec{r}_i, t) + \vec{v}_i \times \vec{B}(\vec{r}_i, t)], \quad (\text{A.1})$$

$$d\vec{r}_i/dt = \vec{v}_i, \quad \vec{p}_i = m_i \vec{v}_i / \sqrt{1 - (\vec{v}_i/c)^2}. \quad (\text{A.2})$$

The $\Phi(r_i, r_j)$ is the Lennard-Jones potential, the \vec{E}_T and \vec{B} are the transverse electric and magnetic fields, respectively, and $\mu_0 = 4\pi \times 10^{-7} \text{W/Am}$ and $\epsilon_0 = 1/\mu_0 c^2$. The Maxwell field equations are written as,

$$\nabla \cdot \vec{E}_L(\vec{r}, t) = (1/\epsilon_0) \sum_{i=1}^N q_i S(\vec{r} - \vec{r}_i), \quad (\text{A.3})$$

$$\partial \vec{B} / \partial t = -\nabla \times \vec{E}_T, \quad (\text{A.4})$$

$$\mu_0 \epsilon_0 \partial \vec{E}_T / \partial t = \nabla \times \vec{B} - \mu_0 \sum_{i=1}^N q_i \vec{v}_{T,i} S(\vec{r} - \vec{r}_i), \quad (\text{A.5})$$

$$\nabla \cdot \vec{B} = 0. \quad (\text{A.6})$$

The magnetic field in plasmas is $\vec{B} = \mu_0 \vec{H}$. The symbol L is the longitudinal electric field, and the shape function $S(\vec{r})$ is prorated to nearest grids. The values are, $c = 2.998 \times 10^8 \text{m/s}$, $e = 1.602 \times 10^{-19} \text{C}$, $m_e = 9.111 \times 10^{-31} \text{kg}$, and $1\text{eV} = 1.602 \times 10^{-19} \text{J}$.

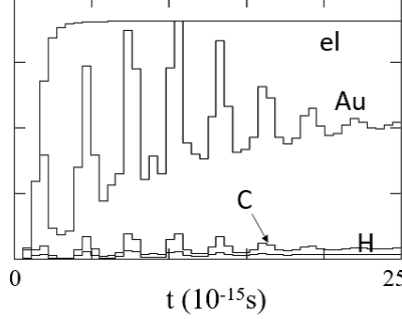


Figure 8: (Appendix B) The electrostatic simulation is shown for the same parameter of Run A4. The maximum and final kinetic energies for the gold ions are 39.6 MeV and 22.7 MeV, respectively, and is 37.2 MeV for electrons in the electrostatic run (the current intensity is too intense). By comparison, those of Run A4 for the electromagnetic run are moderated to be 23.6 MeV and 19.4 MeV for maximum and final values of gold ions, respectively, and 39.7 MeV in electrons.

Appendix B: The Electrostatic Simulation Code

The electrostatic simulation code is used for the low intensity using the first right-hand part of Eq.(6) without electromagnetic fields. It is too much exaggerated for high intensity relativistic cases.

The electrostatic simulation with $\vec{E}_T = \vec{B} = 0$ and $\Delta x = 5\text{\AA}$ is executed for the carbon nanotube accelerator in Fig.8 of Appendix B. The positive ions (protons and gold ions) are accelerated in the parallel direction, while the electrons are accelerated solely in the perpendicular direction. The proton distribution function of V_{\parallel} converges at $V_{\parallel, top} \approx 1.4 \times 10^9 \text{cm/s}$. Pulsation oscillations occur in the 2.7-fs period for the gold and carbon ions, and its highest energy is 40 MeV. The final pulsation oscillation energies are 23 MeV for the gold ions, and 37.2 MeV for the electrons. The difference in the electrostatic code becomes tremendous large in Fig.8, compared to the electromagnetic case in 10^{22}W/cm^2 of Fig.6. .

The electrostatic simulation code is appropriate in the laser intensity not exceeding 10^{18}W/cm^2 .

References

- [1] S. S. Bulanov, A. Brantov, V. Yu. Bychenkov, V. Chvykov, G. Kalinchenko, T. Matsuoka, P. Rousseau, S. Reed, V. Yanovsky, D. W. Litzenberg, and A. Maksimchuk, *Med. Phys.*; 35 (2008) 1770.
- [2] T. Ditmire, J. Zweiback, V. P. Yanovsky, T. E. Cowan, G. Hays, and K. B. Wharton, *Nature*, 398 (1999) 489.
- [3] M. Roth, T. E. Cowan, M. H. Key, S. P. Hatchett, C. Brown, W. Fountain, J. Johnson, D. M. Pennington, R. A. Snavely, S. C. Wilks, K. Yasuike, H. Ruhl, P. Pegoraro, S. V. Bulanov, E. M. Campbell, M. D. Perry, and H. Powell, *Phys. Rev. Lett.*, 86 (2001) 436.
- [4] S. C. Wilks, A. B. Langdon, T. E. Cowan, M. Roth, S. Singh, S. Hatchett, M. H. Key, D. Pennington, A. MacKinnon, and R. A. Snavely, *Phys. Plasmas*, 8 (2001) 542.
- [5] T. E. Cowan, J. Fuchs, H. Ruhl, A. Kemp, P. Audebert, M. Roth, R. Stephens, I. Barton, A. Blazevic, E. Brambrink, J. Cobble, J. Fernandez, J. C. Gauthier, M. Geissel, M. Hegelich, J. Kaae, S. Karsch, G. P. Le Sage, S. Letzring, M. Manclossi, S. Meyroneinc, A. Newkirk, H. Pepin, and N. Renard-LeGalloudec, *Phys. Rev. Lett.*, 92 (2004) 204801.
- [6] B. M. Hegelich, B. J. Albright, J. Cobble, K. Flippo, S. Letzring, M. Paffett, H. Ruhl, J. Schreiber, R. K. Schulze, and J. C. Fernandez, *Nature*, 439 (2006) 441
- [7] H. Daido, M. Nishiuchi, and A. S. Pirozhkov, *Rep. Prog. Phys.*, 75 (2012) 056401.
- [8] M. Murakami and M. Tanaka, *Applied Phys. Letters*, 102 (2013) 163101.
- [9] Y. T. Kim, K. Ohshima, K. Higashimine, T. Uruga, M. Takata, H. Suematsu, and T. Mitani, *Angew. Chem., Int. Ed.*, 45 (2006) 407.
- [10] P. Mulser and D. Bauer, *High power laser-matter interaction*, Springer, Heidelberg, 2010, Chap.7.
- [11] D. Frenkel and B. Smit, *Understanding Molecular Simulation - From Algorithms to Applications*, 2nd edition, Academic Press, United Kingdom, 2001.

- [12] J. A. McCammon and S. C. Harvey, Dynamics of Proteins and Nucleic Acids, Cambridge University Press, 2012 (original 1987).
- [13] M. Deserno and C. Holm, J. Chem. Phys. 109 (1998) 7694.
- [14] M. Tanaka, and M. Sato, J. Chem. Phys., 126 (2007) 034509.
- [15] M. Tanaka and A. Yu. Grosberg, J. Chem. Phys., 115 (2001) 567.
- [16] M. Tanaka and A. Yu. Grosberg, Euro. Phys. J., E7 (2002) 371.
- [17] M. Tanaka, Phys. Review, E68 (2003) 061501.
- [18] Y. Rabin and M. Tanaka, Phys. Rev. Letters, 94 (2005) 148103.
- [19] M. Tanaka, A. Yu. Grosberg, V. S. Pande, and T. Tanaka, Phys. Review, E56 (1997) 5798.
- [20] S.C.Wilks, Physics Plasmas 5 (1993) 2603.
- [21] B-n. Jiang, The Least-Squares Finite Element Method: Theory and Applicatons in Computational Fluid Dynamics and Electrodynamics, Springer, Berlin, 1998.
- [22] J. U. Brackbill, Numerical hydrodynamics for high-beta plasmas, Methods in Computational Physics, edited by B. Adler, S. Feldbach, and M. Rotenberg, Vol. 16 Controlled Fusion, Academic Press, New York, 1976.
- [23] M. Tanaka, J. Comput. Phys., 107 (1993) 124.
- [24] M. Tanaka, Comput. Phys.Commun., 87 (1995) 117.
- [25] M. Tanaka, Phys. Plasmas, 3 (1996) 4010.
- [26] C. J. Subich, J. Comput. Phys., 294 (2015) 297.
- [27] M. Uzunca, B. Karaszen, T. Kkseyhan, Applied Math. Comput., 292 (2017) 9.
- [28] Computation at Lawrence Livermore National Laborotory, at <https://computation.llnl.gov/>,
- [29] M. Murakami and M. Tanaka, Phys. Plasmas, 15 (2008) 082702.
- [30] L. D. Landau and E. M. Lifshitz, The Classical Theory of Fields, Fourth Revised English Edition, Course of Theoretical Physics volume 2, Butterworth Heinemann, New York, 1987.

- [31] R. Heras, European J. Physics, 38 (2017) 055203.
- [32] F. Matteo and J. G. Steven, The Design and Implementation of FFTW3, Proceedings of the IEEE, 93 (2005) 216; at <http://www.fftw.org/>.
- [33] R. Courant, K. Friedrichs, and H. Levy, IBM J. Res. Develop., 11 (1967 [1928]) 215.
- [34] E. Fermi, Nuclear Physics, Chap.1, A Course Given by Enrico Fermi at the University of Chicago, 1974 [1950].